



RESEARCH ARTICLE

10.1029/2022JF006718

Key Points:

- First integration of multiple coastal subsidence monitoring techniques at one site
- High-resolution records from co-located optical fiber strainmeters and GPS instruments corroborate one another
- The site exhibits isostatic subsidence with a potential role of fluid extraction and negligible compaction

Supporting Information:

Supporting Information may be found in the online version of this article.

Correspondence to:

M. A. Zumberge,
mzumberge@ucsd.edu

Citation:

Zumberge, M. A., Xie, S., Wyatt, F. K., Steckler, M. S., Li, G., Hatfield, W., et al. (2022). Novel integration of geodetic and geologic methods for high-resolution monitoring of subsidence in the Mississippi Delta. *Journal of Geophysical Research: Earth Surface*, 127, e2022JF006718. <https://doi.org/10.1029/2022JF006718>

Received 15 APR 2022
Accepted 18 AUG 2022








Author Contributions:

Conceptualization: Mark A. Zumberge, Frank K. Wyatt, Michael S. Steckler, William Hatfield, Timothy H. Dixon, Mead Allison, Torbjörn E. Törnqvist
Data curation: William Hatfield
Formal analysis: Surui Xie, Guandong Li, William Hatfield, Timothy H. Dixon, Jonathan G. Bridgeman, Elizabeth L. Chamberlain, Torbjörn E. Törnqvist
Funding acquisition: Michael S. Steckler, Timothy H. Dixon, Mead Allison, Torbjörn E. Törnqvist
Investigation: Mark A. Zumberge, Surui Xie, Frank K. Wyatt, Michael S. Steckler, Guandong Li, William Hatfield, Donald

© 2022. The Authors.

This is an open access article under the terms of the [Creative Commons Attribution License](https://creativecommons.org/licenses/by/4.0/), which permits use, distribution and reproduction in any medium, provided the original work is properly cited.

Novel Integration of Geodetic and Geologic Methods for High-Resolution Monitoring of Subsidence in the Mississippi Delta

Mark A. Zumberge¹ , Surui Xie¹ , Frank K. Wyatt¹ , Michael S. Steckler², Guandong Li³, William Hatfield¹ , Donald Elliott¹, Timothy H. Dixon⁴ , Jonathan G. Bridgeman³, Elizabeth L. Chamberlain⁵ , Mead Allison³, and Torbjörn E. Törnqvist³ 

¹Scripps Institution of Oceanography, University of California San Diego, La Jolla, CA, USA, ²Lamont-Doherty Earth Observatory, Columbia University, New York, NY, USA, ³Department of Earth and Environmental Sciences, Tulane University, New Orleans, LA, USA, ⁴School of Geosciences, University of South Florida, Tampa, FL, USA, ⁵Soil Geography and Landscape Group, Wageningen University, Wageningen, The Netherlands

Abstract Land-surface subsidence is a major contributor to land loss in many river deltas. New approaches yielding high-resolution data are needed to parse the relevant driving forces. In 2016, we established a novel “subsidence superstation” ~2 km from the Mississippi River in coastal Louisiana (USA) to measure compaction in a global reference frame as a function of depth in Holocene sediments and deeper subsidence. The site features three borehole optical fiber strainmeters to obtain continuous records of displacement between ~1.3 m below the surface and depths of ~11, 25, and 38 m. These data are complemented by an adjacent station providing hydrologic data and near-surface compaction. We also installed three GPS antennas, one of which is mounted to a rod cemented into the Pleistocene basement. A core from one of the boreholes provides insight into the sediment properties of the entire Holocene succession. Five years of records reveal the compaction rate in the material between 1.3 and 38 m is likely less than 0.25 mm/yr. The GPS records yield a subsidence rate of 2.5 mm/yr regardless of the depth of the anchor, thus corroborating the low compaction rates observed by the strainmeters. The new instrumental records show that current subsidence at this location is governed mostly by deformation of the Pleistocene or underlying strata rather than compaction of Holocene material, with the exception of the uppermost meter. The methodology represents an important new approach to mapping subsidence rates at varying depths, providing insight into the mechanisms governing delta subsidence.

Plain Language Summary It is important to learn about the rate and causes of land subsidence along low-lying coastlines and deltas where a large fraction of the world's population lives. In the Mississippi Delta, sediment deposited during the last ~11,000 years (Holocene) has gradually compacted under its own weight. Constraining the path of the Mississippi River with levees over the past century has prevented deposition of new sediment over most of the delta, causing the land surface to drop with respect to sea level, increasing the threat from inundation by seawater. We measured the compaction of a nearly 40 m thick sediment layer at one site in the Mississippi Delta using a combination of optical fiber strainmeters in boreholes to several depths and GPS antennas mounted near the land surface and to deeper points. We found that the subsidence at our site, which occurs at a rate of several mm per year, is caused by very shallow (of order 1 m) and very deep (below 40 m) processes and is not driven by compaction of the bulk of the 38 m thick Holocene layer.

1. Introduction

Coastal lowlands and river deltas, which rise less than 10 m above sea level, are particularly vulnerable to the climate-change effects forecast for the 21st century and beyond, including the threat of inundation by accelerating sea-level rise and increases in the severity of tropical storm surges. Most large deltas are receiving insufficient sediment to maintain themselves (Giosan et al., 2014). These threats coincide with a worldwide surge in human population in coastal areas. Coastal population centers include multiple megacities, whose inhabitants exceed 10 million. Many of these coastal megacities are located on river deltas that are also hubs and hot spots for agriculture, fisheries, transportation, and hydrocarbon production. Most deltas are subsiding, in many cases at rates exceeding the rate of sea-level rise (e.g., Ericson et al., 2006; Jelgersma, 1996; Syvitski et al., 2009). The

Elliott, Jonathan G. Bridgeman, Elizabeth L. Chamberlain, Mead Allison, Torbjörn E. Törnqvist

Methodology: Mark A. Zumberge, Surui Xie, Frank K. Wyatt, Michael S. Steckler, William Hatfield, Donald Elliott, Timothy H. Dixon, Jonathan G. Bridgeman, Mead Allison, Torbjörn E. Törnqvist

Resources: Timothy H. Dixon, Mead Allison, Torbjörn E. Törnqvist

Software: Surui Xie, William Hatfield

Supervision: Mark A. Zumberge, Torbjörn E. Törnqvist

Validation: Timothy H. Dixon, Elizabeth L. Chamberlain

Writing – original draft: Mark A. Zumberge, Torbjörn E. Törnqvist

Writing – review & editing: Mark A. Zumberge, Surui Xie, Frank K. Wyatt, Michael S. Steckler, Guandong Li, William Hatfield, Timothy H. Dixon, Elizabeth L. Chamberlain, Mead Allison

risk to infrastructure and economies is global and directly affects the nearly 350 million people residing in deltas (Edmonds et al., 2020).

Relative sea-level rise, the combined effect of land subsidence and geocentric sea-level rise, constitutes one of the largest climate-related threats to many deltas, and it is now fully recognized that subsidence is a major if not the dominant factor (Fox-Kemper et al., 2021; Oppenheimer et al., 2019). Nevertheless, the most recent assessment report of the Intergovernmental Panel on Climate Change (IPCC-AR6; Fox-Kemper et al., 2021) indicates low to medium confidence in projections of vertical land motion (including glacial isostatic adjustment) and stresses the need for more detailed studies at the regional scale. Despite numerous recent efforts to better understand the processes that contribute to coastal subsidence, progress has been hindered by the fact that different measurement techniques sometimes produce seemingly conflicting results (e.g., Brown & Nicholls, 2015; Frederick et al., 2019; Steckler et al., 2022), presenting an obstacle to disentangling subsidence drivers. For example, even separating the effect of anthropogenic processes (e.g., groundwater vs. hydrocarbon extraction) may be challenging (Candela & Koster, 2022). To alleviate these problems, multidisciplinary approaches by larger research teams are needed (e.g., Allison et al., 2016; Shirzaei et al., 2021). While it has been recognized for some time that the integration of several complementary monitoring techniques holds the key to significant advances, such efforts have been slow to materialize.

Consequently, there is a pressing need to understand what drives coastal subsidence. Here we report our approach and progress on research at a novel “subsidence superstation” in the Mississippi Delta. The purpose of the subsidence superstation is to integrate multiple methods to monitor subsidence at a single site—something that has to date rarely happened. Notable exceptions are recent studies in the Venice Lagoon (Zoccarato & Da Lio, 2021) and the Ganges-Brahmaputra Delta (Steckler et al., 2022). Here, we build on this work by means of a dedicated experiment where multiple instruments are located at the same site. Our goal is to collect precise measurements of Holocene sediment compaction as a function of depth using vertical strainmeters, augmented by GPS antennas anchored both near the surface and to the Pleistocene basement. We contextualize our findings by examining the local stratigraphy at and near the superstation and compare our results with a long record from a nearby rod surface-elevation table–marker horizon installation. Figure 1 shows the location of the superstation; Figure 2 displays the instruments that were installed. Environmental setting, instrumentation, and the results of the observations are provided below.

Our findings are not only relevant to understand ongoing subsidence rates and mechanisms at this site, which is broadly representative of substantial portions of the Mississippi Delta. The superstation site was deliberately chosen due to its proximity to what will be the world’s largest river diversion (Mid-Barataria Sediment Diversion) planned in the near future (Coastal Protection and Restoration Authority of Louisiana, 2017). This diversion is likely to rapidly increase clastic deposition in the area around the superstation, and will potentially accelerate compaction rates.

2. Environmental Setting

The subsidence superstation is located in a brackish marsh ~2 km from the bank of the Mississippi River near Myrtle Grove, Louisiana (Figure 1). It is near Coastwide Reference Monitoring System (CRMS) installation 0276, data from which are available at <http://lacoast.gov/crms2/home.aspx> (Steyer et al., 2003). CRMS sites record hydrological data, including water height in the marsh, and shallow compaction (generally the uppermost 20–25 m) using rod surface-elevation table–marker horizon (RSET-MH) installations (see Webb et al., 2013, for further details on RSET-MHs).

A marsh drill rig was hired in early 2016 to drill three boreholes at the site (its tracks are visible in the Google Earth view in the inset of Figure 1c). The first borehole is 15 cm in diameter and yielded a continuous core (79.5% recovery) to a depth of about 38 m. The other two boreholes have smaller diameters and terminate at depths of about 25 and 11 m. Optical fiber strainmeters were installed in all three boreholes and each borehole also hosts a GPS station (see Figure 2 and the Instrumentation section).

The shallow stratigraphy of the area near the superstation is shown in a cross section (Figure 3). This is based on hand-drilled cores down to 10–12 m depth. Outside of the artificial levee along the Mississippi River, a ~1 m-thick surficial peat bed occurs throughout this area. Below that, about 10 m of mud-dominated proximal

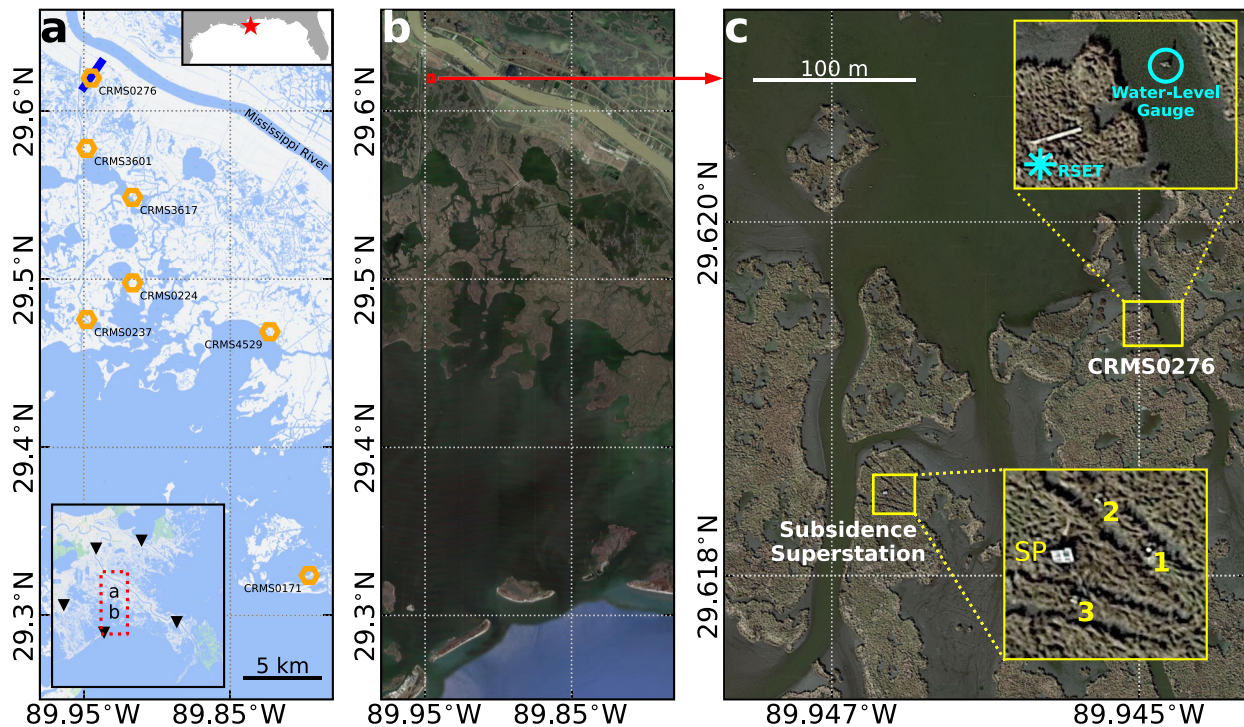


Figure 1. The subsidence superstation and its surroundings. In (a) orange hexagon markers show locations of the water level stations operated by the Coastwide Reference Monitoring System (CRMS), the blue line marks the location of the cross section shown in Figure 3. The top inset shows the location of the study area on the central US Gulf Coast. The dashed red rectangle in the bottom inset outlines the map area shown in (a) and (b) the black triangles indicate the locations of nearby air pressure stations. In (b) a satellite image (from Google Earth) shows the map area in (a). In (c), a close-up image of the outlined box in (b) shows three GPS and strainmeter stations labeled MGW1, MGW2, and MGW3, the solar panels, labeled SP, and a close-up of the CRMS site.

overbank deposits from the modern Mississippi River and a precursor are encountered. This unit also contains a sand bed near its base, along with an intercalated organic-rich unit at 7–8 m depth.

The underlying succession was recovered in the deepest borehole and consists of consolidated Pleistocene mud at the base, overlain by a thin peat bed that reflects the initial rise of the water table due to sea-level rise. It gives way to a thin, sandy bed with abundant shells (Figure S1 in Supporting Information S1). Overlying this is a thick unit of 20–25 m of relatively homogenous clay, interpreted as a shallow marine mud, the uppermost portion of which is shown in the cross section.

3. Instrumentation

The basic components and operation in an optical fiber strainmeter are described in DeWolf et al. (2015) and Zumberge et al. (2018). We review the principles here and describe some details unique to this deployment.

An optical fiber strainmeter consists of a thin (3.8 mm) cable having a sealed stainless-steel tube at its core housing two optical fibers, epoxied to the inside of the cable at both ends. The cable is attached to the bottom of a borehole through a fixture cemented into the base. Then the cable is put under tension to stretch it enough that the enclosed optical fibers are elongated by a small fraction of their length, an amount greater than the negative strain expected to accumulate during the deployment. For this installation, in which we thought significant compaction could occur, we tensioned each fiber cable to 40 pounds, which elongates them by about 0.22% (an 8 cm stretch of the longest one). Changes in the optical fiber lengths caused by displacement of the upper portion of the borehole relative to the base are tracked interferometrically. A laser diode injects light into an optical fiber coupler—part of the light travels along the borehole fiber to a mirror at the bottom end, which reflects the light back up to the coupler. Another portion of the light is sent to a reference fiber wound onto a fused silica mandrel, having a mirror on its end and a length equal to that of the stretched strain-sensing fiber. The combined, reflected light rays interfere with one another in a Michelson configuration, changing from maximum intensity to minimum intensity as

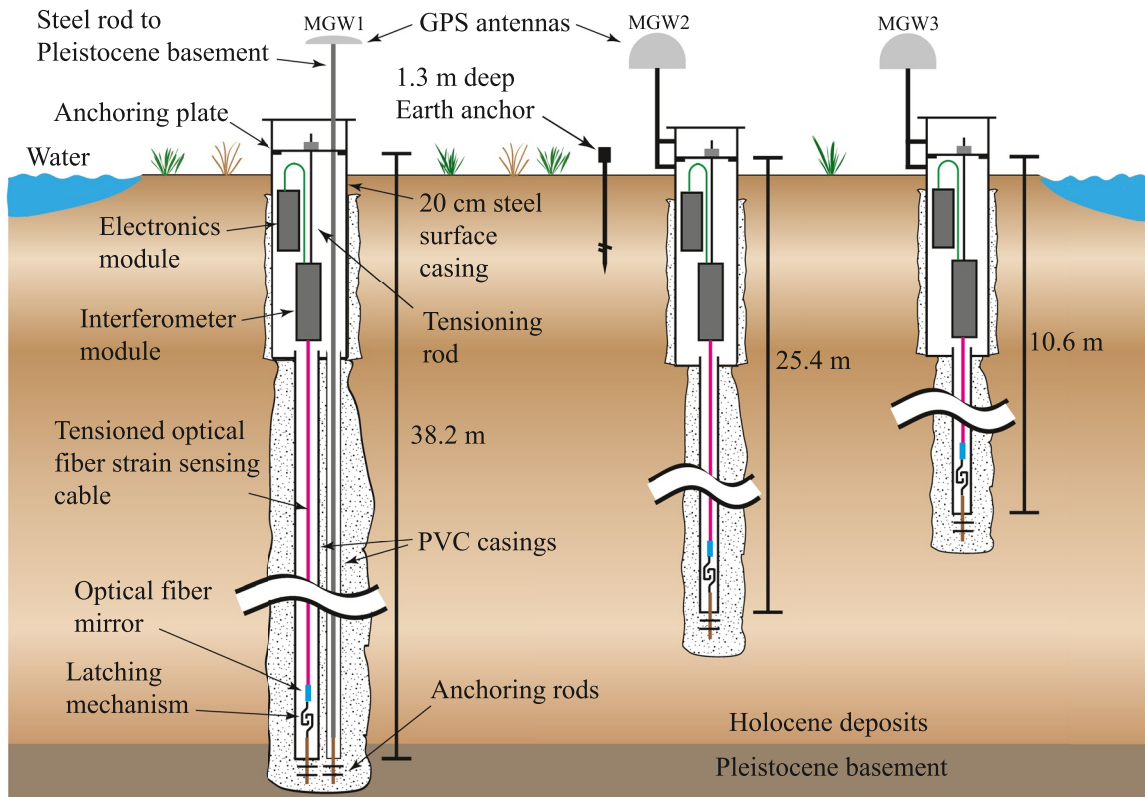


Figure 2. Illustration of the instruments installed at the subsidence superstation. The deepest borehole, which also produced a continuous core, houses two PVC casings: one for an optical fiber strainmeter and a second one for a long rod, which anchors a GPS antenna to the Pleistocene basement. The GPS antennas on the other two boreholes are mounted to pipes welded to the upper ends of the steel surface casings. The heights of all three casings were tracked in a local leveling survey relative to two 1.3 m deep anchor screws a few tens of meters away (see Supporting Information S1). Since no motion was observed between the Earth anchors and the steel casings, the upper limit of the interval tracked by the strainmeters is inferred to be 1.3 m below the surface.

the round-trip optical path changes by one-half wavelength of laser light. In our system, we use 3×3 couplers to generate two fringe signals in quadrature to track increasing and decreasing strain unambiguously (Zumberge et al., 2004). A second interferometer parallels the main interferometer except the fiber in it (inside the same cable) has a different thermal response, allowing us to determine optical length change caused by temperature change and that due to real strain.

As shown in Figure 2, the optical fiber components and the reference mandrel are housed in a sealed sonde 10 cm in diameter and 47 cm in length. The sonde is suspended from a 1.8 m long stainless-steel rod attached to a plate mounted at ground level inside the surface borehole casing. The upper end of the rod is threaded—a mating nut above the plate allows a controlled displacement to be imparted to the sensing cable, establishing a calibration. Six optical fibers run through a sealed, flexible conduit to a second sonde of the same size which houses the laser, photo-detectors, and fringe-signal processing electronics. The processing electronics sample the interferometer fringe signals 50,000 times per second and extract the optical phase. The data are filtered and decimated to a 20 sample per second rate and streamed to a data server at UCSD for examination in near real time and recording. The samples are time-stamped with respect to a GPS-disciplined oscillator within the fringe-signal processing unit. We also record the temperatures of the reference mandrel and the diode laser. This allows correction from signals caused by laser wavelength fluctuation which could result from an imperfect length match between the reference and the strain sensing fibers.

The steel casings cemented into the ground near the surface extend to depths of 2.5 m for the two longer strainmeters and to 3.3 m for the third one. It is difficult to know the exact depth of the top of the effective strain-sensing interval with this arrangement. However, leveling measurements of the heights of the exposed casing tops with respect to two reference points each at a depth of 1.3 m show no significant (i.e., within 1 or 2 mm) displacement over the 5-year course of the experiment (see supporting information Figures S2 and S3 in Supporting

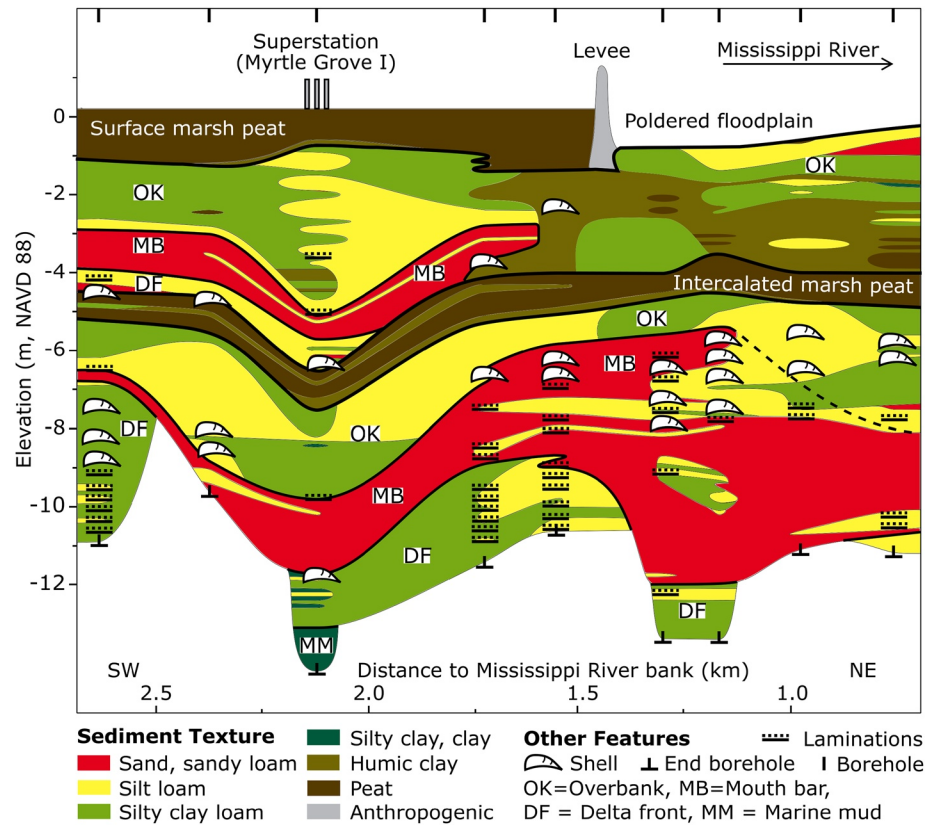


Figure 3. Cross section that includes the Myrtle Grove I core (corresponding to MGW1 in Figure 2) at the subsidence superstation plus adjacent hand-drilled cores, oriented perpendicular to the Mississippi River (location shown by the blue line in Figure 1a). Note the ~1 m thick peat bed at the surface outside the levee, which likely formed after levee construction when the wetland was isolated from the sediment source.

Information S1). Thus it is safe to say that the two surface GPS antennas mounted directly to the casings and the optical fiber strainmeters are equivalently anchored at a depth of 1.3 m. That is, deformation that occurs below 1.3 m would be visible in the GPS and strain records. Compaction of material above 1.3 m would not be detected.

All three borehole strain sensors are powered from solar-charged batteries; each sensor requires around 5 W. A cellular system modem transmits the data over the internet to the central server. The data are held in a ring buffer in the processing electronics to accommodate short interruptions to the data connection. Longer gaps in the records resulted from various failures, sometimes associated with the power system, which in one instance was flooded during Hurricane Barry (July 2019). Gaps present a problem in that the displacement record is relative—there is no way to recover whatever displacement accumulates during a gap when the sensor is unpowered other than aligning the records before and after the gap during a data editing process.

As noted above and shown in Figure 2, three GPS antennas, one associated with each strain sensor, are used to record absolute position. Two of the antennas are mounted to the surface casings. The third, on the deepest borehole, is mounted to a 1.6 cm diameter stainless-steel rod routed through its own PVC conduit to the bottom of the borehole where it is cemented in place. The rod was assembled on site by screwing together 3 m long segments. The uppermost segment exits the borehole casing lid through a low-friction guide and is attached to the third GPS antenna. The receivers used are Trimble NetR9s. The data are collected over the internet and stored at the UNAVCO data archive (<ftp://data-out.unavco.org/pub/rinex/obs>).

The deepest and shallowest strain sensors were deployed in July 2016, the three GPS antennas and receivers were added in August of the same year. The third strainmeter, to intermediate depth, was installed in May 2017. During installation of each strainmeter, a known displacement was imparted to check the calibration by advancing the nut on the threaded rod that supports the interferometer housing. Not long after the third sensor was put in, a different

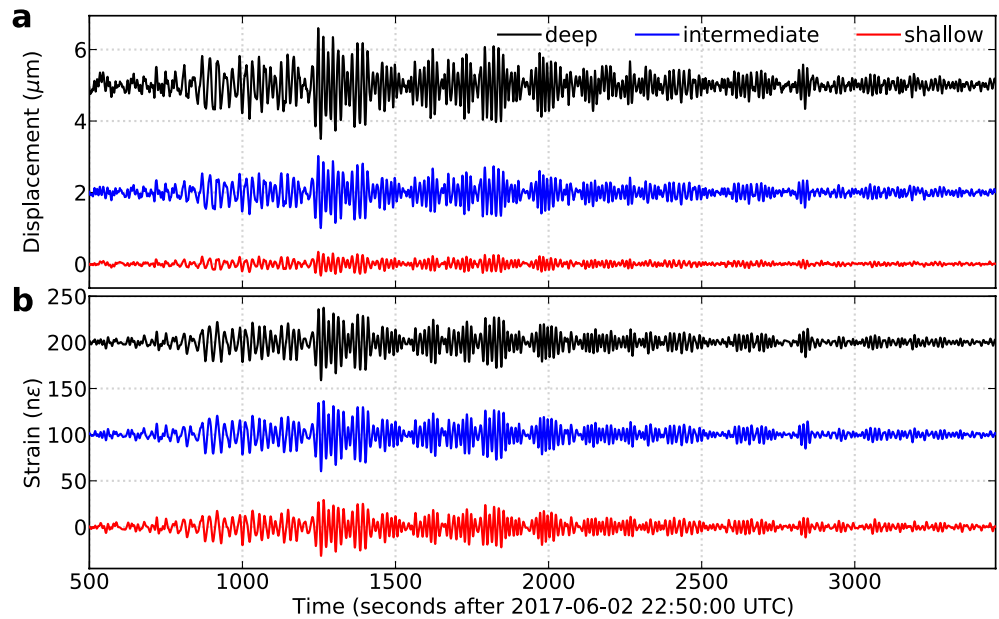


Figure 4. (a) Displacement and (b) strain records for a time interval of ~ 1 hr on 2 June 2017, capturing a magnitude 6.8 earthquake 8,000 km away, with arbitrary offsets added for clarity. Records are bandpass filtered between 0.01 and 0.2 Hz. Note that in these plots, and in subsequent plots showing displacement, arbitrary constant values have been added to each data series, shifting the traces vertically for display clarity (in actuality each begins at zero).

form of instrument check was provided by an M6.8 earthquake in the Aleutian peninsula, southwest Alaska, USA, on 2 June 2017. Figure 4 shows the ~ 1 hr records from all three sensors capturing the event $\sim 8,000$ km away. The upper traces are in units of displacement; these are converted to strain—expected to be the same for all three—in the lower plot.

Some intermediate term results (periods of hours to days) are shown in Appendix A. This includes an interesting relationship between the marsh water level and vertical strain. First, though, we concentrate on the long-term results from the strainmeters and the GPS stations.

4. Long-Term Results From the Optical Fiber Sensors

Figure 5 shows the long-term results from all three optical fiber sensors. The dominant short-period signal in each sensor is related to the local marsh water height, described in detail in Appendix A. There is a clear annual cycle, also associated with the water height. Over the 5-year duration of the experiment, the compaction in the material encompassed by the strainmeter array accumulates to about 1 mm. As stated above, the depth range covered by these measurements begins at 1.3 m below the surface. All three sensors appear to be in agreement with this result, although the intermediate depth sensor did not recover from the power outage associated with Hurricane Barry. A second damaging hurricane (Ida) on 29 August 2021, destroyed the solar power and data telemetry infrastructure. Consequently, our data set ends on that date, slightly more than 5 years since its beginning.

To determine the average slopes of the three strainmeter records in Figure 5, we first subtracted principal components having annual and semiannual periods, to remove the seasonal signals. Then a linear least squares regression was used to fit the remaining time series. The resulting slopes for the shallow, intermediate, and deep strainmeters are -0.06 ± 0.1 mm/yr, -0.06 ± 0.1 mm/yr, and -0.19 ± 0.27 mm/yr, respectively. Uncertainty estimates are described next.

As an important goal of the experiment was to determine the rate of compaction of the Holocene succession, a discussion of the uncertainty in the maximum compaction rate is important. There are two factors which contribute to the uncertainty. One is from the gaps in the time series, the second is from a problem with the temperature compensation in one of the three sensors that started around the beginning of 2020.

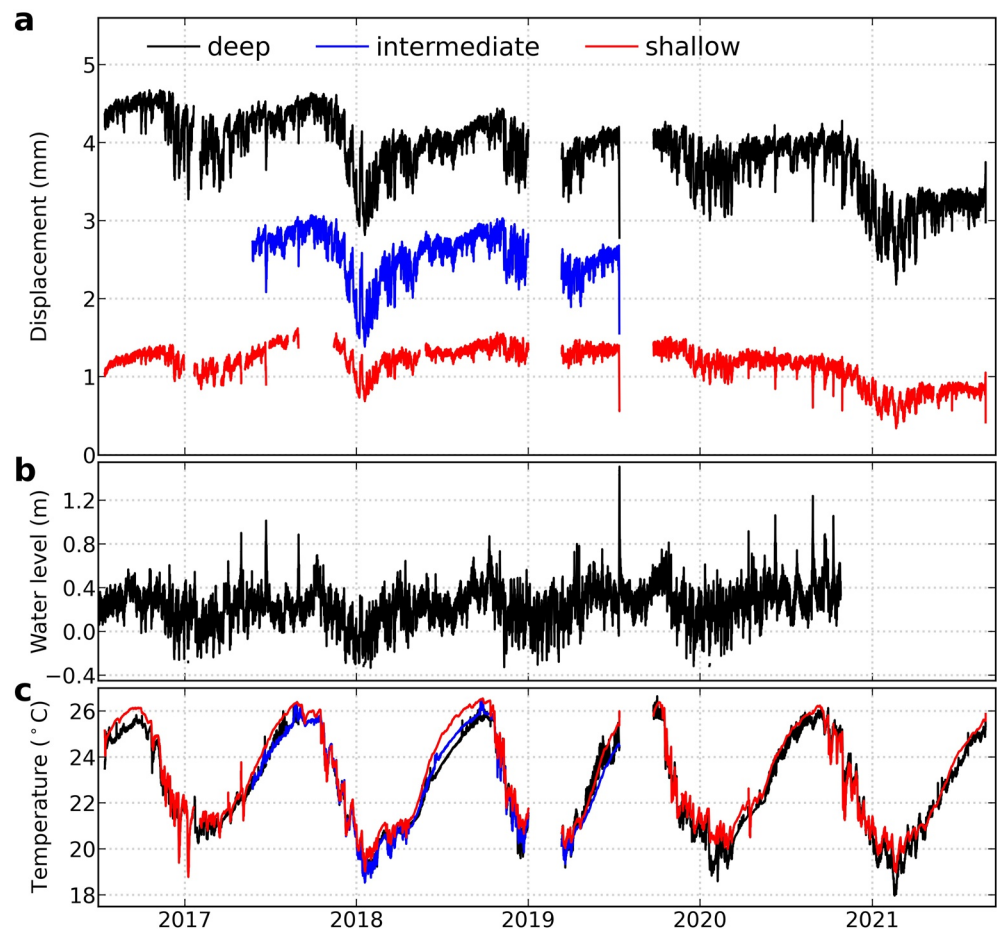


Figure 5. Displacements determined by the three optical fiber strainmeters are shown in (a) with arbitrary offsets added for clarity. Deviations are correlated with water level in the marsh (b); the ground surface rises as the water level rises until the marsh island becomes inundated, after which rising water level causes the elevation to decrease. The most noticeable case is the storm surge from Hurricane Barry in mid-2019, during which the marsh water level rose by ~ 1.5 m in a few hours and the surface height dropped by about 1.2 mm with respect to 38 m depth (shown in more detail in Appendix Figure A1). Plot (c) shows the temperature at a depth of about 2 m inside the three water-filled surface casings.

One data gap, in the shallow sensor, was caused by a problem with a memory card in its signal processor; the other two long gaps were caused by interruptions to the power system and/or the data transmission system. Hurricane Barry caused a storm surge that increased the local water level in the marsh by nearly 1.5 m, flooding the solar power battery charging circuitry. All three sensors show a ~ 1 mm depression of the ground surface caused by the load from the surface water just before the hurricane-induced power failure (see the Appendix A). Editing the data across the gaps is fairly subjective—one aligns the time series after the gap with the series preceding it, trying to avoid the introduction of an artificial offset while observing the trends that might be expected from other years during the annual cycle. We estimate that the uncertainty from each gap is no larger than ~ 0.25 mm, hence the total uncertainty accumulated from the three major gaps amounts to about $\sqrt{3} \times 0.25$ mm = 0.43 mm. Thus, we believe the uncertainty in the slope averaged over 5 years is of order 0.1 mm/yr.

The second problem occurred in the deepest sensor. To understand its level of significance, an explanation of the temperature compensation scheme is required. As described in Zumberge et al. (2018), the temperature coefficient contrast in the two fibers in each strainmeter is fairly small. The temperature correction is derived from observing the difference in displacement recorded by the two fibers. Normally, this difference is not large. However, beginning in 2020 we noticed the temperature inferred from this method showed an unreasonably large drift in the deep strainmeter, indicating that one of its two fibers was producing a slightly erroneous displacement, amplifying the temperature correction to an unrealistic level. We therefore eliminated the temperature correction

for this instrument. Prior to 2020, the difference between the temperature-corrected and non-temperature-corrected slopes is about 0.25 mm/yr. Because of this we increase the uncertainty in the 5-year slope of the deepest sensor to 0.27 mm/yr (the quadrature sum of 0.1 mm/yr and 0.25 mm/yr).

We have some confidence in the long-term stability of the optical fibers. One example comes from a 250 m long tensioned fiber in a borehole at Piñon Flat Observatory in the California desert described in DeWolf et al. (2015). It has been in continuous operation for 7 years and it shows no secular displacement larger than 0.12 mm/yr. Further stability evidence comes from a 575 m test fiber wrapped on a mandrel and kept isolated in one of our basement labs since 1998; it has been stable in length to 0.1 ppm per year during that time, that is, 0.06 mm/yr.

While there is no way to know if the anchor points at the base of the boreholes are stable, the consistency of the results among all of the measurements indicates that they are not moving relative to one another; the earthquake response also confirms good coupling.

One other issue that is important to consider in the assessment of these results is the level of stability of the steel casings. These proved to be surprisingly free from shifting as evidenced both by leveling surveys, shown in Figure S3 in Supporting Information S1, and by the GPS records, described next.

5. GPS Results

GPS data obtained between August 2016 and August 2021 at stations MGW1, MGW2, and MGW3 were analyzed into daily averaged positions using GipsyX software (v.1.6), with orbit and satellite clock products provided by the Jet Propulsion Laboratory (Bertiger et al., 2020). Ocean tide loading corrections were computed on the Onsala Space Observatory website (<http://holt.oso.chalmers.se/loading/>) with the FES2014b model (Lyard et al., 2021). Tropospheric delays were estimated using the VMF1 mapping function (Böhm et al., 2006). Second-order ionospheric effects were corrected using the IONEX model (Kedar et al., 2003). To estimate secular trends, a multi-channel singular spectrum analysis (M-SSA) method was used to remove seasonal oscillations in GPS time series (Walwer et al., 2016). Velocity uncertainties were calculated with the Hector software (Bos et al., 2013), using a power law plus white noise model. Figure 6 is a plot of the processed data.

Note that there were two ~5 mm step changes in early 2017 in the north and east displacement time series of the deep station—no associated step was observed in the vertical component. These resulted because visits to the site required removal of the site's antenna for access to strainmeter components. The steps were edited out from the time series shown, and two Heaviside functions were applied in velocity estimates in least squares regression. The horizontal rates are relative to the North America Plate defined in the ITRF2014 Plate Motion Model.

The average subsidence rate is 2.5 ± 0.3 mm/yr. There is no statistically significant difference in the rates among the three records. Since one of our three GPS antennas is anchored below the Pleistocene-Holocene contact by the 38 m long rod while the other two are mounted to surface casings with effective anchor points at a depth of 1.3 m, and all three GPS systems exhibit the same subsidence rate within the GPS uncertainty (0.3 mm/yr), one must conclude that the sediment between their anchor points is not undergoing significant compaction, that is, compaction of Holocene sediment within this depth range is negligible. This agrees with the results from the optical fiber strainmeters.

6. RSET-MH Results

As previously noted, neither the optical fiber strainmeters nor the GPS instruments are sensitive to compaction within the shallowest strata above about 1.3 m depth. To address this, we examined vertical accretion (VA) and surface-elevation change (SEC) at CRMS site 0276, about 200 m NE of the superstation (Figure 7). While this CRMS site is on a different marsh island, it is likely representative of the situation at the superstation given the laterally continuous stratigraphy (Figure 3). SEC tracks the vertical position of the sediment surface with respect to a rod driven deeply into the sediment measured with an RSET (rod surface elevation table). Surface elevations are measured relative to a horizontal steel arm attached to the top of the driven rod and rotated to average the surface height in the vicinity of the fixed rod twice a year. VA is determined from the varying depths, in cores collected over time, of Marker Horizons (MH—thin layers of readily identified marking material added sequentially in time to the wetland surface). Shallow subsidence (SS) is the difference between SEC and

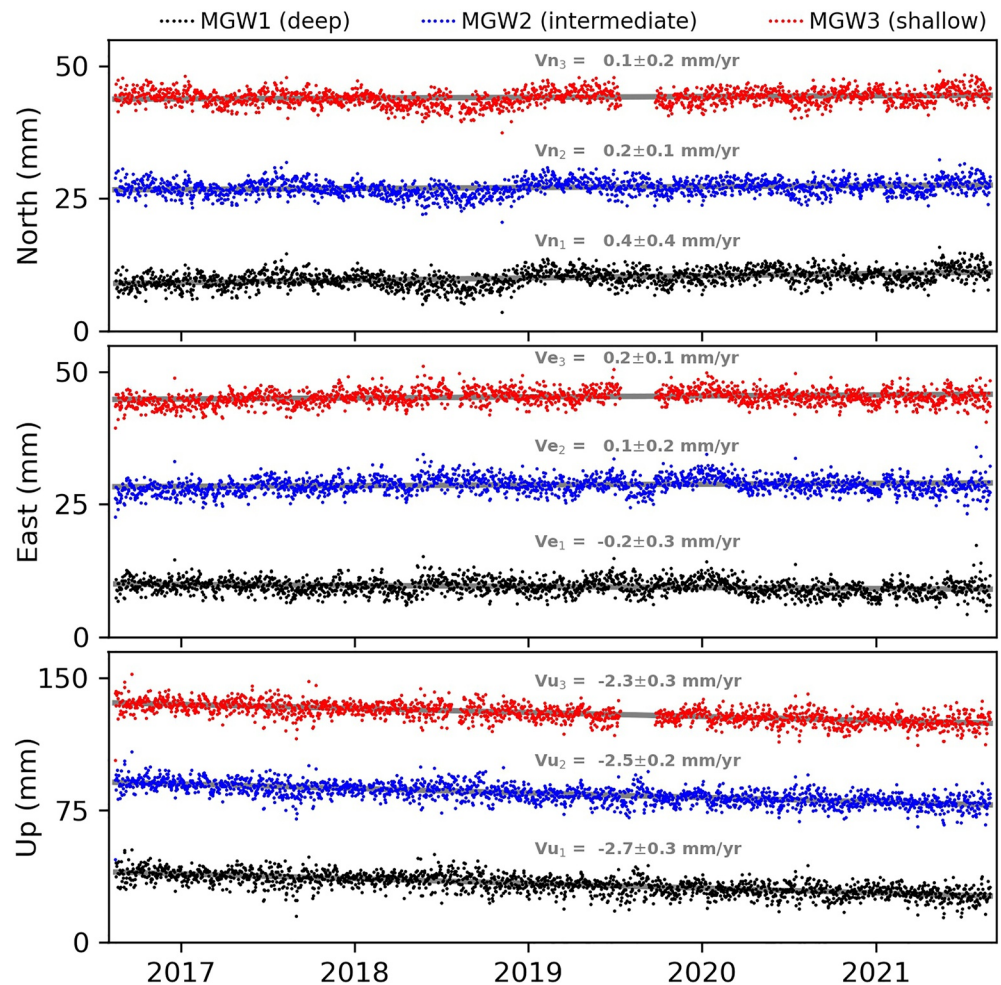


Figure 6. GPS time series with seasonal variations removed using a multichannel singular spectrum analysis method. Displacements are arbitrarily offset for clarity. Gray lines are best fitting lines for secular velocities.

VA (e.g., Cahoon, 2015; Webb et al., 2013). In other words, if the rate at which material is being added to the surface (VA) is greater than the rate the surface elevation is observed to actually increase (SEC), then SS must explain the difference. The CRMS 0276 RSET has a rod length that extends 26.5 m below the surface, that is, comparable to the anchor depth of the strainmeter that occupies the intermediate well (MGW2). The RSET-MH method allows the present-day SS rate to be determined by subtracting the SEC rate from the VA rate. Jankowski et al. (2017) reported a SS rate of 0.4 mm yr^{-1} (i.e., essentially zero) for this site for the period 2008–2015. Since this precedes the time interval captured by the superstation instruments, we now expand on this analysis and take advantage of a much richer record of accretion rates from four instead of just one set (known as a plot set, PS) of marker horizons. First, we examine the longest available record (corresponding to PS1) which provides a SS rate of 2.5 mm yr^{-1} (Figure 7a). This suggests an increase of the SS rate in more recent years. The four sets of marker horizons (PS1–PS4) that capture the time period 2015–2021 show some variability between VA rate records, yet all of them exhibit higher values than the SEC rate (5.7 mm yr^{-1} ; Figure 7b) for the corresponding time interval. The SS rates from the four plot sets are 7.7, 4.6, 2.8, and 3.7 mm yr^{-1} , respectively, resulting in an average value of $4.7 \pm 2.1 \text{ mm yr}^{-1}$. We stress that caution is in order due to the noisy nature of these data and the associated uncertainties, and the reliance on just one site. Nevertheless, the fact that all four MH records exhibit an increase in SS rate lends some confidence to our interpretation.

We speculate that the increase in SS rate may be partly related to the spike in accretion associated with Hurricane Isaac (2012) that led to rapid deposition in this portion of the Mississippi Delta (Bianchette et al., 2016), a process associated with enhanced SS and that can also be seen in Figure 7a. It is worth noting, however, that

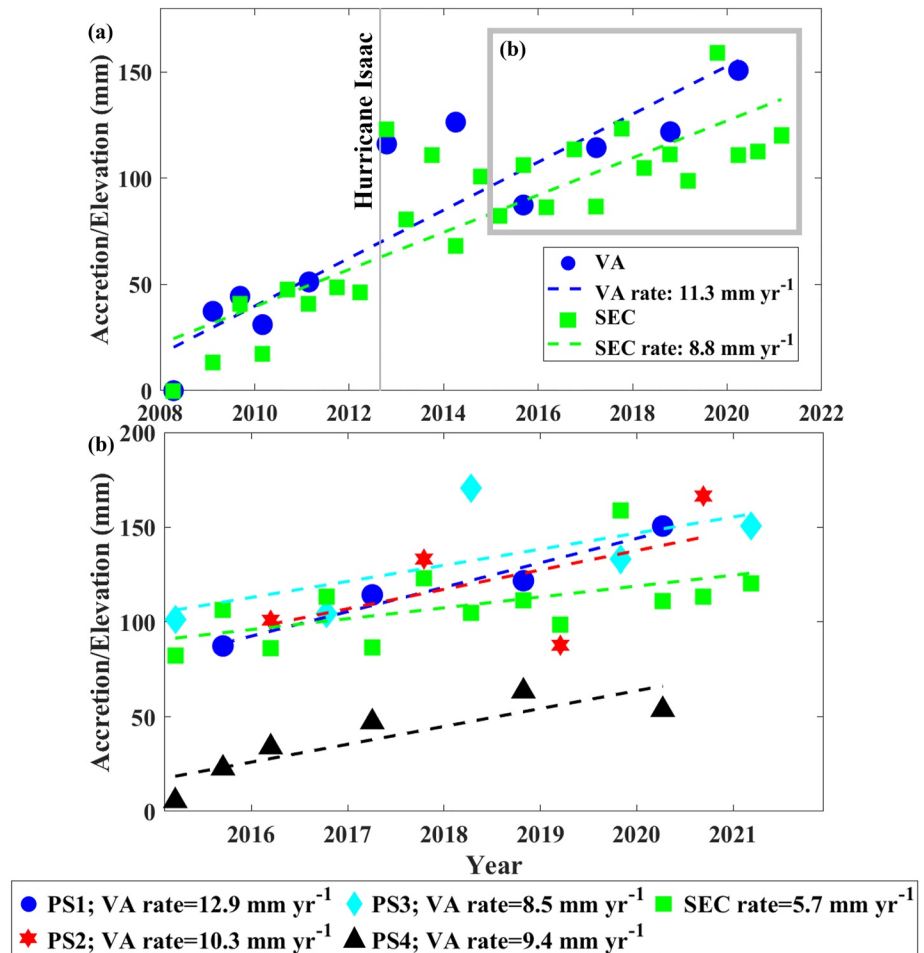


Figure 7. Surface-elevation change (SEC) and vertical accretion (VA) at the CRMS0276 site, 200 m NE from the superstation (see Figure 1c). Illustrated in (a) is the full record (2008–2021) based on VA measurements from one plot set (PS1) whereas (b) shows the time period that broadly corresponds to the superstation instrumental records (2015–2021), based on four plots (PS1–4) for VA measurements.

the calculated SS rate is still lower than the average SS rate in coastal Louisiana (6.8 mm yr⁻¹) as reported by Jankowski et al. (2017). Since the data from the superstation imply virtually no compaction between 1.3 and 38.2 m below the wetland surface, the suggested increase of the SS rate for the period 2015–2021 from the RSET-MH data indicates that the vertical land motion mainly occurred in the shallowest subsurface. Keogh et al. (2021) recently demonstrated that most sediment compaction in coastal Louisiana wetlands occurs in the top 1–3 m, shortly after the initial deposition over organic-rich coastal strata. Most significantly, geotechnical modeling by Keogh et al. (2021) showed that compaction due to loading of the Holocene sediment column at the superstation site (at present or in the future) will be accommodated for 60%–70% by the peat bed that constitutes the uppermost 1 m. Nevertheless, this model would still predict a higher rate of compaction than we observe for the 1.3–38.2 m interval even with their uncertainties; 30%–40% of 2.6 mm/yr (the lowest SS rate considering its uncertainty) yields a predicted rate for the deeper layers of a minimum of 0.8–1.0 mm/yr, while our observation (with its uncertainty) would be at most 0.46 mm/yr. Given the location of the RSET-MH measurements (~200 m away from the superstation) and limitations of the geotechnical model, we would argue that the results from the different methods are likely reconcilable.

7. Synthesis and Implications

While this may not presently be the case at the superstation, it is well documented that Holocene sediment compaction dominates the total present-day subsidence in most of coastal Louisiana (e.g., Chamberlain et al., 2021; Jankowski et al., 2017; Karegar et al., 2015; Keogh et al., 2021; Meckel et al., 2006; Penland & Ramsey, 1990; Törnqvist et al., 2008). Previously buried (Pleistocene) sediments do not significantly decompact with unloading (Chapman, 1983). Further compaction only occurs when overburden pressure exceeds previous levels. Thus, during the Holocene, compaction has primarily occurred in the Holocene-aged sediments and not in the underlying older strata.

Keogh and Törnqvist (2019) pointed out that GPS measurements in coastal Louisiana generally do not account for compaction of the upper ~15 m of Holocene sediment because they are anchored more deeply. Karegar et al. (2020) used GPS reflectometry to show this effect can contribute an additional 3–6 mm/yr to the subsidence budget in the delta. Byrnes et al. (2019) report a number of GPS-derived rates of vertical land motion from a wider region around the superstation, but only one of their instruments (~40 km inland from the superstation) is anchored in the Pleistocene like our deep well; it shows a rate of 0.7 mm/yr.

Furthermore, Byrnes et al. (2019) argued that GPS instruments that rest on unanchored and unsleeved monuments capture the total subsidence signal (i.e., including shallow subsidence) due to downdrag forces produced by sediment compaction. Since the superstation features GPS instruments supported by a sleeved rod in one case (MGW1) and attached to the unsleeved surface casing in the other cases (MGW2 and MGW3), our results offer an excellent opportunity to test this hypothesis. If downdrag due to sediment compaction is a significant factor (as shown by the RSET-MH data), one would expect the latter two instruments to exhibit higher velocities than the anchored and sleeved instrument associated with the deep well. However, the velocities found for the three instruments are indistinguishable. Likewise, the three strainmeters exhibit indistinguishable (and extremely small) rates, indicating a negligible downdrag effect.

Glacial isostatic adjustment (GIA) has been predicted to contribute subsidence of order 1 mm/yr along the central US Gulf Coast (Peltier et al., 2015; Wolstencroft et al., 2014). Sedimentary isostatic adjustment (SIA) also needs to be considered, reflecting the long-term viscoelastic response to the large sediment input from the Mississippi River and the favored model scenario run by Wolstencroft et al. (2014) predicts about 1.5 mm/yr due to GIA plus SIA at the superstation, although this is not a finely tuned model run. Kuchar et al. (2018) jointly inverted for combined GIA and SIA using a recently developed model that computes ocean loading in a gravitationally self-consistent manner for pre-defined ice and sediment loading models (Dalca et al., 2013). Their model predicts the combined effects of GIA and SIA results in subsidence of order 1 mm/yr at the coast (i.e., seaward of the superstation), with a maximum subsidence rate of about 2.8 mm/yr considering model uncertainty. Using Kuchar et al.'s (2018) best subsidence estimate (1 mm/yr) suggests that nearly half of our observed deep subsidence may be explained from GIA and SIA. Thus, we consider other potential processes.

Another potential source of subsidence below the Pleistocene surface is fluid withdrawal from oil and gas production. Morton et al. (2006) and Chang et al. (2014) reported evidence for enhanced local subsidence due to hydrocarbon production based on releveling surveys in a different portion of the Mississippi Delta. The depressurization during and after hydrocarbon extraction typically extends beyond the oil and gas fields. These studies showed that the associated subsidence bowls have diameters in the 5–10 km range. There are 37 oil and gas wells within 8 km of the superstation that have been active since 1977, all with depths <4,500 m (Figure 8). Although the monthly production in this region has declined significantly since the late 1970s, the associated subsidence might persist for decades after well abandonment (Chang et al., 2014).

Faulting is another plausible driver of deep subsidence. For example, recent fault activity 50–80 km north of the superstation has been observed (Hopkins et al., 2022). However, studies of fault slip rates in coastal Louisiana over geologic time scales generally show low rates, typically <0.1 mm/yr (e.g., Frederick et al., 2019; Shen et al., 2017). Finally, we cannot preclude the possibility that the underlying Pleistocene sediments are compacting and contribute to our subsidence signal, although this is likely to be very small (e.g., Frederick et al., 2019).

Notwithstanding the overall modest subsidence rates at the superstation site, this may change in the near future due to the Mid-Barataria Sediment Diversion that aims to build and maintain deltaic (wet) land in the area surrounding the superstation (Coastal Protection and Restoration Authority of Louisiana, 2017). When implemented,

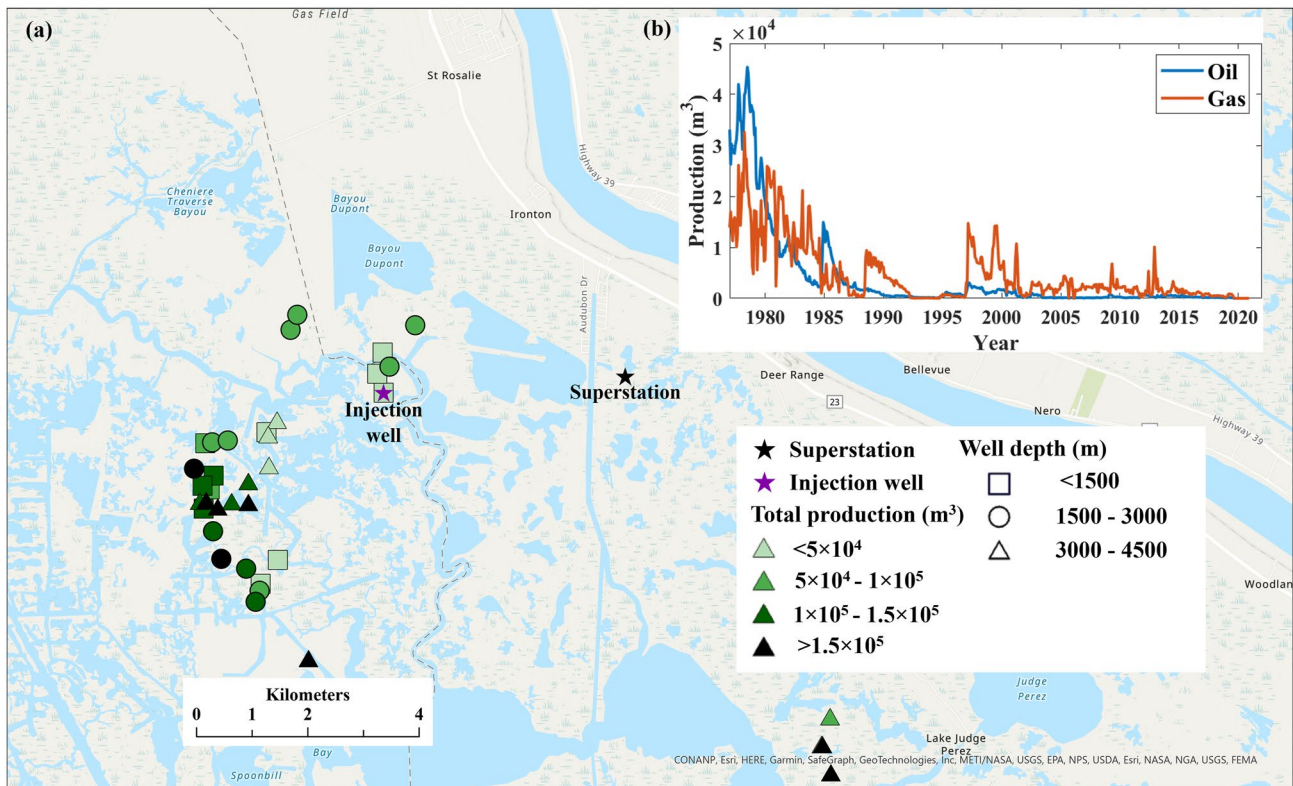


Figure 8. Oil and gas extraction records from the area surrounding the subsidence superstation. Illustrated in (a) is a map of combined oil and gas (total) production for all active wells since 1977 whereas (b) shows monthly oil and gas production for all wells, respectively. (Source: <https://www.sonris.com/>).

this river diversion will bring a significant increase in clastic sediment, likely accelerating shallow compaction (e.g., Chamberlain et al., 2021). Our data provide a valuable pre-diversion baseline to assess the impacts of the Mid-Barataria Sediment Diversion with regard to subsidence.

Despite the relatively low compaction rates observed today below the surficial peat bed, there is ample evidence that conditions were different in the past. Bridgeman (2018) demonstrated on the order of 5 m of vertical motion due to compaction during the past $\sim 3,000$ years, mainly associated with loading due to overbank deposition by the Mississippi River. Based on an analysis of bulk density data, Keogh et al. (2021) estimated that the Myrtle Grove I core has lost about 8 m of thickness in the past $\sim 11,000$ years, the time of accumulation of this sediment succession. They used geotechnical modeling to demonstrate that the sediment column as it exists today is prone to compaction in the future due to loading by the sediment diversion, mainly the surface peat and to a lesser extent the marine mud.

For the 5 year period (2016–2021) the GPS time series define a reliable rate of 2.5 ± 0.3 mm/yr deep-seated downward vertical motion, uncontaminated by shallow sediment compaction, and attributable to a combination of GIA, SIA, fluid extraction, tectonics, and compaction of older sediments. Both the GPS data and the strainmeter records demonstrate that sediment compaction within the Holocene succession is negligible below the uppermost 1.3 m. The nearby RSET-MH data suggest that this near surface unit may have experienced appreciable compaction during the project period. Adding the shallow compaction inferred from CRMS 0276 to the deep processes we have directly measured here implies that the site may have experienced ~ 7 mm/yr of total subsidence during this time, slightly less than the average rate (9 ± 1 mm/yr) reported for coastal Louisiana (Nienhuis et al., 2017). These conditions will likely change when sediment delivery from the planned Mid-Barataria Sediment Diversion reaches the superstation area.

Robust coastal prediction requires better and more integrated measurements and models, and this science must be linked with its socio-economic implications (e.g., Allison et al., 2016; Shirzaei et al., 2021). While the present investigation does not provide subsidence projections for the study site and its surroundings, it nonetheless

constitutes a step in this direction. The novel combination of subsidence time series offers new prospects for rigorous model testing. For example, we provide new constraints for GIA models such as those discussed above, and the compaction measurements will aid the calibration and/or validation of state-of-the-art geomechanical models (e.g., Zoccarato & Teatini, 2017) that target coastal lowlands. Carefully designed networks of subsidence superstations can provide the spatial dimension needed to tune predictive models, with the eventual goal to bridge the gap with IPCC-style projections of relative sea-level rise in these vulnerable settings.

8. Conclusions

We used optical fiber strainmeters and GPS to obtain high-resolution records of subsidence at a continuous experimental station in a Mississippi Delta marsh. This approach is novel, particularly considering that strainmeters are presently underutilized in delta subsidence research, and GPS stations are anchored at variable and often poorly known levels, providing limited observations of shallow subsidence. We offer new insights into the practical use, value, and uncertainties of this combination of techniques. The optical fiber strainmeters are sensitive to micron level displacement of the surface with respect to their anchor points, a depth of 38 m for the deepest of the three, and the GPS records vertical motion precise to 0.3 mm/yr.

Integrating across different methods targeting different depths, plus the high resolution of the records, allows us to parse the deep and shallow processes that contribute to subsidence at our site. Compaction of the Holocene deposits is less than 0.25 ± 0.27 mm/yr (excluding the uppermost 1 m peat layer). The rate of subsidence of a point at 1.3 m depth with respect to a global reference frame, measured by the GPS instruments, is 2.5 ± 0.3 mm/yr. The near-zero compaction rate of the Holocene material between 1.3 and 38 m indicates that subsidence at this station is not due to compaction in this interval, but rather results from deformation of material within or below the Pleistocene strata. Shallow compaction between the surface and 1.3 m cannot be detected by our measurements although we can infer it from nearby RSET-MH measurements. We observe compaction of the Holocene material when loaded, with a coefficient of around 1–2 mm for a load equivalent to 1 m of water (see Appendix A). This will be a major factor if new sediment is deposited in the region, such as is proposed by the Mid-Barataria Sediment Diversion project. Our new results show that processes occurring below the Holocene succession contribute substantially to subsidence at this site, and that compaction within the Holocene is presently constrained to a very shallow surface layer.

Appendix A: Short Period Results from the Optical Fiber Strainmeters

A significant correlation between atmospheric pressure and vertical strain was not apparent in the strainmeter data. However, as can be seen in Figure 5, large increases in the marsh water level are associated with downward displacement of the surface, most evident from the large storm surge in mid-2019 that ultimately flooded the power system. Closer examination of the records reveals a curious phenomenon: when the mean level of the marsh water is below a certain threshold, there is a positive correlation between water height and ground displacement (increasing water height causes increasing ground height). The correlation changes sign when the threshold is exceeded.

Figure A1 displays this clearly: the upper panel shows the displacement for a 2-week period prior to the Hurricane Barry, which provided the largest vertical deformation signal. The middle panel plots two series: the thick gray trace is the marsh water level, the red trace is the water level “mirrored” about a threshold (0.3 m—black line) found empirically. Water level above this threshold is given a sign change and appropriate offset to reflect the data around the threshold. The “mirrored” red trace is highly correlated with the ground displacements measured by all three strainmeters, with linear correlation coefficients of 0.95, 0.97, and 0.93. At maximum water height the ratio of vertical height change measured by the deep sensor (in mm) to mean water level change (in m) is -1.0 mm/m (as the water level increases the ground is displaced downward). At the lowest water levels the ratio is $+1.3$ mm/m (the ground rises as the water level rises).

The reversal of sign in the correlation between local water height and vertical strain can be explained by two competing mechanisms. A complete model of this phenomenon will be quite complicated and is beyond the scope of this work, however a simple order-of-magnitude calculation supports our explanation. First, the geometry of the site is important. The sensors are installed on an island in the marsh. The water level varies mainly with a

diurnal period and the island has a characteristic lateral dimension of 100 m and on average is about 0.3 m above the water surface. Its vertical relief is measured in centimeters and is surrounded by large areas of slightly lower, always-submerged terrain (see Figure 1c). At the highest water levels the island surface becomes fully submerged. The drawing in Figure 2 depicts the water level just below the island surface.

Two competing processes are responsible for the relationship between water level and vertical strain. First, when the water level is below the island surface (island not fully submerged) rising water level affects the Holocene layer (spanned by our deepest strainmeter) in two ways: the hydrostatic pressure throughout the formation increases, compressing the Holocene layer causing it to elastically shrink, which tends to lower the island surface. However, accompanying this affect is a competing one—as the water level rises, more of the upper island becomes buoyantly lifted, releasing some load from the formation allowing it to rise. This is the larger effect yielding uplift as the water level rises. When the water level rises over the top of the island (island fully submerged), there is no longer a change in buoyancy with increasing water height and only the first mechanism is active, so the land sinks as the water level rises.

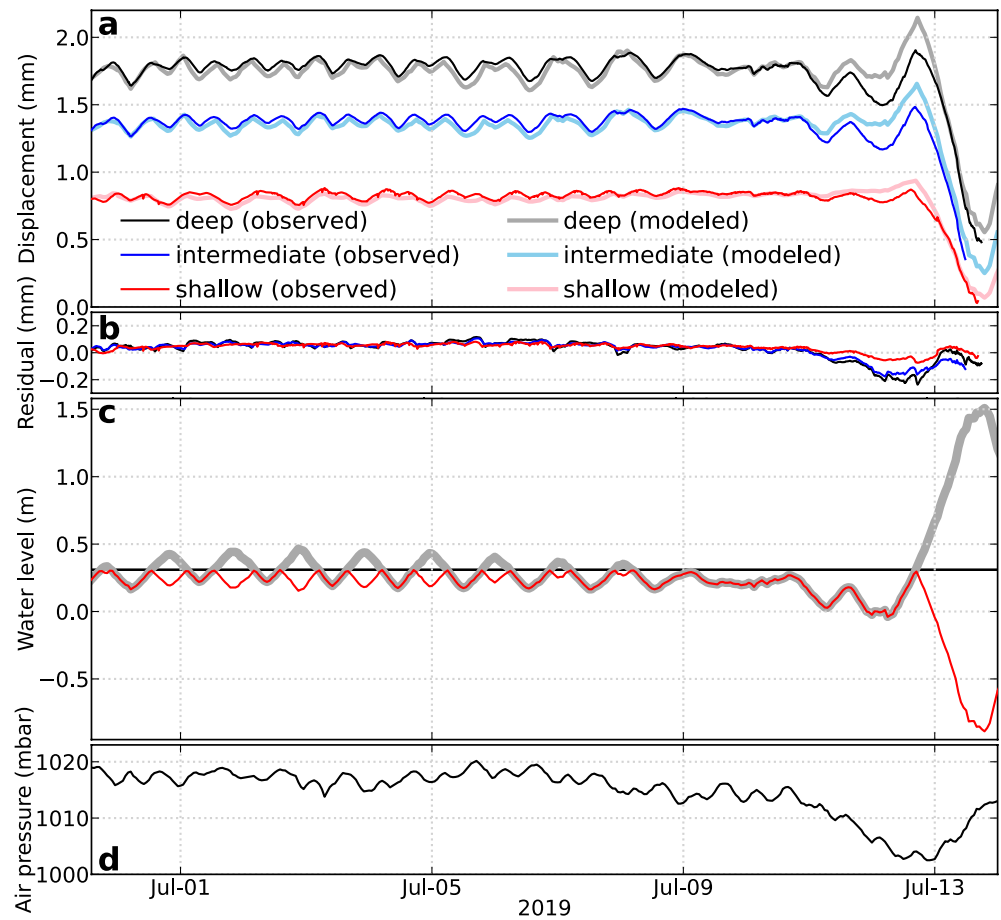


Figure A1. A demonstration of the correlation between water height change and ground height change. The water level (gray line in (c)) is “mirrored” about a threshold (solid horizontal line in (c)), approximately at a level where the marsh island becomes flooded. The red trace in (c) is the “mirrored” series, scaled and reproduced in (a) as the lighter colored fits to the solid traces in (a) which are the strainmeter records. The “mirrored” red trace is well correlated with the ground displacement. The linear correlation coefficients are 0.95, 0.97, and 0.93 for the long, intermediate and short fiber strainmeters, respectively. In (b) the residuals are plotted after subtraction of the modeled displacements. The fits to the three strainmeters are improved by allowing slightly different thresholds and scaling factors for each strainmeter (the one in (c) is representative). Also note that the water level record was constructed by analyzing the records from many nearby Coastwide Reference Monitoring System (CRMS) stations, calculating appropriate time delays from each, and then averaging them—this was needed because the closest CRMS station went off scale when the water level dropped below 0 m (a description of this routine is in the supporting information Figures S4–S7 in Supporting Information S1).

A model that is little more than a dimensional analysis leads to an expression like:

$$\frac{\Delta z}{z} \sim \frac{\Delta p}{E}$$

for the compression effect, where Δz is ground level change, $\Delta p = \rho gh$ is pressure change from a height h of water having density ρ (g is local gravity), E and z are the Young's modulus and thickness of the Holocene succession. For $\Delta p = 10$ kPa (the pressure change from a 1 m layer of water), $z = 39$ m, and $\Delta z = 1$ mm, we obtain $E = 0.39$ GPa (a value that falls within the middle of a large range quoted in the literature for clay, e.g., Telford et al., 1990). The sign change occurs when the free surface of the island is not flooded and an additional, similar expression is needed, including density of the Holocene material, roughly twice that of water, describing the varying load from changing buoyancy but opposite in sign relative to the compression effect. Further work with a finite element model that takes into account layers with different porosities, permeabilities, and elastic characteristics is needed to confirm this speculative model.

Data Availability Statement

The GPS data are available from the UNAVCO data repository. Strainmeter data are available in the Harvard Dataverse Repository (Hatfield, 2022). RSET-MH and water level data are available from the CRMS network (<http://lacoast.gov/crms2/home.aspx>).

References

- Allison, M., Yuill, B., Törnqvist, T., Amelung, F., Dixon, T., Erkens, G., et al. (2016). *Global risks and research priorities for coastal subsidence*. Eos, 97. <https://doi.org/10.1029/2016EO055013>
- Bertiger, W., Bar-Sever, Y., Dorsey, A., Haines, B., Harvey, N., Hemberger, D., et al. (2020). GipsyX/RTGx, a new tool set for space geodetic operations and research. *Advances in Space Research*, 66(3), 469–489. <https://doi.org/10.1016/j.asr.2020.04.015>
- Bianchette, T. A., Liu, K.-B., Qiang, Y., & Lam, N. S.-N. (2016). Wetland accretion rates along coastal Louisiana: Spatial and temporal variability in light of Hurricane Isaac's impacts. *Water*, 8(1), 1. <https://doi.org/10.3390/w8010001>
- Böhm, J., Werl, B., & Schuh, H. (2006). Troposphere mapping functions for GPS and very long baseline interferometry from European Centre for Medium-Range Weather Forecasts operational analysis data. *Journal of Geophysical Research*, 111(B2). <https://doi.org/10.1029/2005jb003629>
- Bos, M. S., Fernandes, R. M. S., Williams, S. D. P., & Bastos, L. (2013). Fast error analysis of continuous GNSS observations with missing data. *Journal of Geodesy*, 87(4), 351–360. <https://doi.org/10.1007/s00190-012-0605-0>
- Bridgeman, J. G. (2018). *Understanding Mississippi Delta subsidence through stratigraphic and geotechnical analysis of a continuous Holocene core at a subsidence superstation*. Tulane University.
- Brown, S., & Nicholls, K.-B. (2015). Subsidence and human influences in mega deltas: The case of the Ganges-Brahmaputra-Meghna. *Science of the Total Environment*, 527–528, 362–374. <https://doi.org/10.1016/j.scitotenv.2015.04.124>
- Byrnes, M. R., Britsch, L. D., Berlinghoff, J. L., Johnson, R., & Khalil, S. (2019). Recent subsidence rates for Barataria Basin, Louisiana. *Geo-Marine Letters*, 39(4), 265–278. <https://doi.org/10.1007/s00367-019-00573-3>
- Cahoon, D. R. (2015). Estimating relative sea-level rise and submergence potential at a coastal wetland. *Estuaries and Coasts*, 38(3), 1077–1084. <https://doi.org/10.1007/s12237-014-9872-8>
- Candela, T., & Koster, K. (2022). The many faces of anthropogenic subsidence. *Science*, 376(6600), 1381–1382. <https://doi.org/10.1126/science.abn3676>
- Chamberlain, E. L., Shen, Z., Kim, W., McKinley, S., Anderson, S., & Törnqvist, T. E. (2021). Does load-induced shallow subsidence inhibit delta growth? *Journal of Geophysical Research: Earth Surface*, 126(11), e2021JF006153. <https://doi.org/10.1029/2021JF006153>
- Chang, C., Mallman, E., & Zoback, M. (2014). Time-dependent subsidence associated with drainage-induced compaction in Gulf of Mexico shales bounding a severely depleted gas reservoir. *American Association of Petroleum Geologists Bulletin*, 98(6), 1145–1159. <https://doi.org/10.1306/11111313009>
- Chapman, R. E. (1983). Chapter 3: Compaction of sediment and sedimentary rocks, and its consequences. In R. E. Chapman (Ed.), *Petroleum geology, developments in petroleum science* 16 (pp. 41–65). Elsevier.
- Coastal Protection and Restoration Authority of Louisiana. (2017). Louisiana's comprehensive master plan for a sustainable coast. 171.
- Dalca, A. V., Ferrier, K. L., Mitrovica, J. X., Perron, J. T., Milne, G. A., & Creveling, J. R. (2013). On postglacial sea level—III. Incorporating sediment redistribution. *Geophysical Journal International*, 194(1), 45–60. <https://doi.org/10.1093/gji/ggt089>
- DeWolf, S., Wyatt, F. K., Zumbege, M. A., & Hatfield, W. (2015). Improved vertical optical fiber borehole strainmeter design for measuring Earth strain. *Review of Scientific Instruments*, 86(11), 114502. <https://doi.org/10.1063/1.4935923>
- Edmonds, D. A., Caldwell, R. L., Brondizio, E. S., & Siani, S. M. O. (2020). Coastal flooding will disproportionately impact people on river deltas. *Nature Communications*, 11(1), 4741. <https://doi.org/10.1038/s41467-020-18531-4>
- Ericson, J. P., Vörösmarty, C. J., Dingman, S. L., Ward, L. G., & Meybeck, M. (2006). Effective sealevel rise and deltas: Causes of change and human dimension implications. *Global and Planetary Change*, 50(1–2), 63–82. <https://doi.org/10.1016/j.gloplacha.2005.07.004>
- Fox-Kemper, B., Hewitt, H. T., Xiao, C., Aðalgeirsdóttir, G., Drijfhout, S. S., Edwards, T. L., et al. (2021). Ocean, cryosphere and sea level change. In V. Masson-Delmotte, P. Zhai, A. Pirani, S. L. Connors, C. Pean, S. Berger, et al. (Eds.) *Climate change 2021: The physical science basis. Contribution of working group I to the sixth assessment report of the intergovernmental panel on climate change* (pp. 1211–1361). Cambridge University Press.
- Frederick, B. C., Blum, M., Fillon, R., & Roberts, H. (2019). Resolving the contributing factors to Mississippi Delta subsidence: Past and present. *Basin Research*, 31(1), 171–190. <https://doi.org/10.1111/bre.12314>
- Giosan, L., Syvitski, J., Constantinescu, S., & Day, J. (2014). Protect the world's deltas. *Nature*, 516(7529), 31–33. <https://doi.org/10.1038/516031a>

- Hatfield, W. (2022). *Strain data*, Harvard Dataverse. <https://doi.org/10.7910/DVN/SZNNHHB>
- Hopkins, M., Lopez, J., & Songy, A. (2022). Coastal subsidence due to faults: Insights from elevation profiles of vehicular bridges, southeastern Louisiana, U.S.A. *Journal of Coastal Research*, 38(1), 52–65. <https://doi.org/10.2112/jcoastres-d-21-00015.1>
- Jankowski, K. L., Törnqvist, T. E., & Fernandes, A. M. (2017). Vulnerability of Louisiana's coastal wetlands to present-day rates of relative sea-level rise. *Nature Communications*, 8(1), 14792. <https://doi.org/10.1038/ncomms14792>
- Jelgersma, S. (1996). Land subsidence in coastal lowlands. In J. D. Milliman & B. U. Haq (Eds.) *Sea-level rise and coastal subsidence. Causes, consequences, and strategies* (pp. 47–62). Kluwer.
- Karegar, M. A., Dixon, T. H., & Malservisi, R. (2015). A three-dimensional surface velocity field for the Mississippi Delta: Implications for coastal restoration and flood potential. *Geology*, 43(6), 519–522. <https://doi.org/10.1130/g36598.1>
- Karegar, M. A., Larson, K. M., Kusche, J., & Dixon, T. H. (2020). Novel quantification of shallow sediment compaction by GPS interferometric reflectometry and implications for flood susceptibility. *Geophysical Research Letters*, 47(14), e2020GL087807. <https://doi.org/10.1029/2020gl087807>
- Kedar, S., Hajj, G. A., Wilson, B. D., & Heflin, M. B. (2003). The effect of the second order GPS ionospheric correction on receiver positions. *Geophysical Research Letters*, 30(16), 1829. <https://doi.org/10.1029/2003gl017639>
- Keogh, M. E., & Törnqvist, T. E. (2019). Measuring rates of present-day relative sea-level rise in low-elevation coastal zones: A critical evaluation. *Ocean Science*, 15(1), 61–73. <https://doi.org/10.5194/os-15-61-2019>
- Keogh, M. E., Törnqvist, T. E., Kolker, A. S., Erkens, G., & Bridgeman, J. G. (2021). Organic-matter accretion, shallow subsidence, and river delta sustainability. *Journal of Geophysical Research: Earth Surface*, 126(12), e2021JF006231. <https://doi.org/10.1029/2021jf006231>
- Kuchar, J., Milne, G., Wolstencroft, M., Love, R., Tarasov, L., & Hijma, M. (2018). The influence of sediment isostatic adjustment on sea level change and land motion long the US Gulf coast. *Journal of Geophysical Research: Solid Earth*, 123(1), 780–796. <https://doi.org/10.1002/2017jb014695>
- Lyard, F. H., Allain, D. J., Cancet, M., Carrère, L., & Picot, N. (2021). FES2014 global ocean tide atlas: Design and performance. *Ocean Science*, 17(3), 615–649. <https://doi.org/10.5194/os-17-615-2021>
- Meckel, T. A., Ten Brink, U. S., & Williams, S. J. (2006). Current subsidence rates due to compaction of Holocene sediments in southern Louisiana. *Geophysical Research Letters*, 33(11), L11403. <https://doi.org/10.1029/2006gl026300>
- Morton, R. A., Bernier, J. C., & Barras, J. A. (2006). Evidence of regional subsidence and associated interior wetland loss induced by hydrocarbon production, Gulf Coast region, USA. *Environmental Geology*, 50(2), 261–274. <https://doi.org/10.1007/s00254-006-0207-3>
- Nienhuis, J. H., Törnqvist, T. E., Jankowski, K. L., Fernandes, A. M., & Keogh, M. E. (2017). A new subsidence map for coastal Louisiana. *Geological Society of America Today*, 27(9), 58–59. <https://doi.org/10.1130/gsatg337gw>
- Oppenheimer, M., Glavovic, B. C., Hinkel, J., Van de Wal, R., Magnan, A. K., Abd-Elgawad, A., et al. (2019). Sea level rise and implications for low-lying islands, coasts and communities. In H.-O. Pörtner, D. C. Roberts, V. Masson-Delmotte, P. Zhai, M. Tignor, E. Poloczanska, et al. (Eds.), *IPCC special report on the ocean and cryosphere in a changing climate* (pp. 321–445). Cambridge University Press.
- Peltier, W. R., Argus, D. F., & Drummond, R. (2015). Space geodesy constrains ice age terminal deglaciation: The global ICE-6G_C (VM5a) model. *Journal of Geophysical Research: Solid Earth*, 120(1), 450–487. <https://doi.org/10.1002/2014jb011176>
- Penland, S., & Ramsey, K. E. (1990). Relative sea-level rise in Louisiana and the Gulf of Mexico: 1908–1988. *Journal of Coastal Research*, 6, 323–342.
- Shen, Z., Dawers, N. H., Törnqvist, T. E., Gasparini, N. M., Hijma, M. P., & Mauz, B. (2017). Mechanisms of late quaternary fault throw-rate variability along the north central Gulf of Mexico coast: Implications for coastal subsidence. *Basin Research*, 29(5), 557–570. <https://doi.org/10.1111/bre.12184>
- Shirzaei, M., Freymueller, J., Törnqvist, T. E., Galloway, D. L., Dura, T., & Minderhoud, P. S. J. (2021). Measuring, modelling and projecting coastal land subsidence. *Nature Reviews Earth & Environment*, 2(1), 40–58. <https://doi.org/10.1038/s43017-020-00115-x>
- Steckler, M. S., Oryan, B., Wilson, C. A., Grall, C., Nooner, S. L., Mondal, D. R., et al. (2022). Synthesis of the distribution of subsidence of the lower Ganges-Brahmaputra Delta, Bangladesh. *Earth-Science Reviews*, 224, 103887. <https://doi.org/10.1016/j.earscirev.2021.103887>
- Steyer, G. D., Sasser, C. E., Visser, J. M., Swenson, E. M., Nyman, J. A., & Raynie, R. C. (2003). A proposed coast-wide reference monitoring system for evaluating wetland restoration trajectories in Louisiana. *Environmental Monitoring and Assessment*, 81(1/3), 107–117. <https://doi.org/10.1023/a:1021368722681>
- Syvitski, J. P. M., Kettner, A. J., Overeem, I., Hutton, E. W. H., Hannon, M. T., Brakenridge, R. G., et al. (2009). Sinking deltas due to human activities. *Nature Geoscience*, 2(10), 681–686. <https://doi.org/10.1038/ngeo0629>
- Telford, W. M., Geldart, L. P., & Sheriff, R. E. (1990). *Applied geophysics*, Cambridge university press.
- Törnqvist, T. E., Wallace, D. J., Storms, J. E. A., Wallinga, J., Van Dam, R. L., Blauw, M., et al. (2008). Mississippi Delta subsidence primarily caused by compaction of Holocene strata. *Nature Geoscience*, 1(3), 173–176. <https://doi.org/10.1038/ngeo129>
- Walwer, D., Calais, E., & Ghil, M. (2016). Data-adaptive detection of transient deformation in geodetic networks. *Journal of Geophysical Research: Solid Earth*, 121(3), 2129–2152. <https://doi.org/10.1002/2015jb012424>
- Webb, E. L., Friess, D. A., Krauss, K. W., Cahoon, D. R., Guntenspergen, G. R., & Phelps, J. (2013). A global standard for monitoring coastal wetland vulnerability to accelerated sea-level rise. *Nature Climate Change*, 3(5), 458–465. <https://doi.org/10.1038/nclimate1756>
- Wolstencroft, M., Shen, Z., Törnqvist, T. E., Milne, G. A., & Kulp, M. (2014). Understanding subsidence in the Mississippi Delta region due to sediment, ice, and ocean loading: Insights from geophysical modeling. *Journal of Geophysical Research: Solid Earth*, 119(4), 3838–3856. <https://doi.org/10.1002/2013jb010928>
- Zoccarato, C., & Da Lio, C. (2021). The Holocene influence on the future evolution of the Venice Lagoon tidal marshes. *Communications Earth & Environment*, 2(1), 77. <https://doi.org/10.1038/s43247-021-00144-4>
- Zoccarato, C., & Teatini, P. (2017). Numerical simulations of Holocene salt-marsh dynamics under the hypothesis of large soil deformations. *Advances in Water Resources*, 110, 107–119. <https://doi.org/10.1016/j.advwatres.2017.10.006>
- Zumberge, M. A., Berger, J., Dzieciuch, M. A., & Parker, R. L. (2004). Resolving quadrature fringes in real time. *Applied Optics*, 43(4), 771–775. <https://doi.org/10.1364/ao.43.000771>
- Zumberge, M. A., Hatfield, W., & Wyatt, F. K. (2018). Measuring seafloor strain with an optical fiber interferometer. *Earth and Space Science*, 5(8), 371–379. <https://doi.org/10.1029/2018ea000418>